Structural distortion and collinear-to-helical magnetism transition in rutile-type FeO$_2$

Shiyou Liang and Rong Yu [*]

National Center for Electron Microscopy in Beijing, School of Materials Science and Engineering, Key Laboratory of Advanced Materials of Ministry of Education of China, State Key Laboratory of New Ceramics and Fine Processing, Tsinghua University, Beijing 100084, People's Republic of China

The recent discovery of FeO$_2$ under high pressures has aroused great interest. With the fully anisotropic density-functional theory$+U$ method, we present a predictive study of structural and magnetic transitions of rutile-type FeO$_2$ after reproducing the experimental spiral wave vector in isostructural β-MnO$_2$. A second-order structural distortion (tetragonal to orthorhombic) involving octahedral rotation occurs at a critical pressure of $3 \sim 4$ GPa. From a global search in the Brillouin zone, the ground-state spin order of rutile-type FeO$_2$ is found to be collinear below 22 GPa and transforms to a helix at higher pressures. The phases remain insulating throughout the whole pressure range, with a change from an indirect gap in the high-spin state to a direct gap in the low-spin state. Our work extends the fundamental understanding of iron oxides and provides schemes that treat strongly correlated magnetic systems in a proper and effective way.

DOI: 10.1103/PhysRevB.102.014448

I. INTRODUCTION

Strongly correlated transition-metal oxides (TMOs) are known for the entanglement of charge, orbital, and spin degrees of freedom in d electrons [1,2]. Governed by a certain crystal symmetry which belongs to one of the 230 space groups, lattice may also come into play in the form of electron-phonon interactions [1]. Dynamical stability imposes a strong limit on structures that can be possibly crystallized into for a given stoichiometry [3]. Generally the thermodynamic ground states among them construct phase diagrams as a function of external conditions. However, due to retarded dynamics, metastable phases can be experimentally achieved under ambient conditions, such as γ-Fe$_2$O$_3$ and anatase-TiO$_2$ [4–6]. For strongly correlated systems, electronic and magnetic phase transitions further complicate the phase diagrams [1], making the theoretical prediction a big challenge.

Rutile-type compounds (space group: $P4_2/mnm$) with the simple MO$_2$ stoichiometry are one of the best-known groups of TMOs. For instance, rutile TiO$_2$ is a wide-band-gap (3.1 eV) semiconductor [7,8] which has been studied extensively as a photocatalyst [9,10]. CrO$_2$, one of the prototypical half-metallic ferromagnet with $T_c = 392 \sim 396$ K, finds application in magnetic recording media and spintronic devices [11,12]. Even more interestingly, upon cooling, the metallic rutile-type VO$_2$ undergoes a phase transition at 340 K and becomes a monoclinic insulator (M1 phase). This Peierls-assisted Mott transition makes VO$_2$ a promising phase-change material [13], which has motivated masses of theoretical and experimental research.

The rutile framework seems to fail for iron oxides. Actually it is only in recent years that the FeO$_2$ stoichiometry has come to light, ever since the discovery of a very stable pyrite phase (space group: $Pa\bar{3}$) at high pressure (76 GPa) and high temperature (1800 K) by Hu *et al.* [14]. Most of later works further elucidated the structural details and properties of this new phase [15–19], while the possibilities of being stabilized in other symmetries under different pressures were also unraveled [17,18]. Density-functional theory (DFT) calculations by Lu *et al.* [17] show that in the pressure range of $30 \sim 40$ GPa, the enthalpies of phases in $P4_2/mnm$, $Pbcn$, and $P2/m$ symmetries are all comparable with that of pyrite-type FeO$_2$. X-ray diffraction spectra identify the metastable rutile phase in $P4_2/mnm$ and α-PbO$_2$-type structure in $Pbcn$ upon decompression to 41 and 31 GPa, coexisting with the pyrite phase [17].

Because the rutile phase has a considerable energetic advantage over the others in the low-pressure regime, a single phase with novel properties is expected in the recovered specimen. Although it is predicted to be a ferromagnetic half metal at 31 and 41 GPa [17], no experimental results have been reported yet. Magnetism in strongly correlated systems is of extreme complexity and should be addressed with discretion. For example, rutile-type β-MnO$_2$ takes on a helical magnetic order below $T_N = 92$ K [20,21], whereas early DFT$+U$ calculations predicted a ferromagnetic ground state due to the negligence of full anisotropy in Coulomb and exchange interactions [22]. On the other hand, electron correlation and lattice distortion might also play essential roles in the pressure-driven phase transitions, analogous to the temperature-driven metal-insulator transition (MIT) in VO$_2$ [13]. Thus, a systematic study of the pressure-dependent phase diagram is necessary for rutile-type FeO$_2$.

In this work, starting from a predictive study on the spin order of β-MnO$_2$, we carefully explore the magnetic ground states of rutile-type FeO$_2$ with varying pressure. The related phase transitions and physical properties are discussed.

[*]ryu@tsinghua.edu.cn

II. COMPUTATIONAL METHODS

We employ the DFT+U approach introduced by Liecht-enstein *et al.* [23] with the Perdew-Burke-Ernzerhof [24] exchange-correlation functional and projected augmented-wave [25] potentials as implemented in the Vienna *Ab initio* Simulation Package (VASP) [26,27]. Instead of using $U_{\text{eff}} = U{-}J$ as simplified by Dudarev [28], Liechtenstein's scheme offers a fully anisotropic treatment of the Coulomb and ex-change matrices by taking reasonable U and J values dis-tinctly. It has proved necessary for the description of complex magnetic and electronic structures of strongly correlated sys-tems such as binary manganese oxides [29,30]. Our calcula-tions adopt $U = 2.8$ eV, $J = 1.2$ eV for β-MnO$_2$, which was found to capture the helical magnetism [29], and $U = 5$ eV, $J = 0.8$ eV for rutile-type FeO$_2$ as in the previous work [15]. The cutoff energy for plane waves is 500 eV throughout the calculations, with the convergence criteria being 10^{-6} eV for electronic self-consistent runs and 0.005 eV/Å for ionic steps. The Brillouin-zone integrals are evaluated using special k points generated by the Monkhorst-Pack scheme [31].

The primitive cell is adopted for spin-spiral calculations by virtue of the generalized Bloch theorem [32]. Firstly, full and volume-fixed relaxations are carried out to search for the ground states at ambient pressure and high pressures, respectively. After finding the structural and magnetic ground states in different pressure regimes, the energy-volume rela-tions are computed with fixed spin orders and then fitted by the Birch-Murnaghan equation of state (EOS) [33]. With two pressure-induced phase transitions identified, the evolution of electronic properties and lattice stability is studied using re-optimized magnetic supercells. For pressures of 0 and 20 GPa (31 GPa), the supercells consist of two (three) primitive cells in the **c** direction, with an intrinsically collinear (noncollinear) spin order. The bond valence sums [34] are estimated to ex-amine the oxidation states in ambient FeO$_2$. Elastic constants are obtained with the universal linear-independent coupling strains (ULICS) method [35] and phonon dispersions are gen-erated with the finite displacement method as implemented in the PHONOPY code [36].

III. MAGNETIC GROUND STATE OF β-MnO$_2$

Before dealing with FeO$_2$, we revisit the β-MnO$_2$ system with the generalized Bloch-wave scheme. Previously, the heli-cal magnetic order has only been approached using a magnetic supercell which is constructed according to the experimental configuration [29]. However, it is unclear if this spin helix can be directly predicted by theoretical calculations.

Spin spirals may be conveniently modeled using a general-ization of the Bloch condition [32]:

$$\begin{bmatrix} \psi_{\mathbf{k}}^{\uparrow}(\mathbf{r} + \mathbf{R}) \\ \psi_{\mathbf{k}}^{\downarrow}(\mathbf{r} + \mathbf{R}) \end{bmatrix} = e^{i\mathbf{k}\cdot\mathbf{R}} \begin{pmatrix} e^{-i\mathbf{q}\cdot\mathbf{R}/2} & 0 \\ 0 & e^{i\mathbf{q}\cdot\mathbf{R}/2} \end{pmatrix} \begin{bmatrix} \psi_{\mathbf{k}}^{\uparrow}(\mathbf{r}) \\ \psi_{\mathbf{k}}^{\downarrow}(\mathbf{r}) \end{bmatrix}, \quad (1)$$

where $\mathbf{q}$ is the spiral propagation wave vector typically con-fined in the first Brillouin zone and $\mathbf{R}$ is a *lattice vector* in real space. This strategy has been applied to the fcc γ-Fe system, well reproducing the experimental wave vector of $2\pi/a\times$ (0.1, 0, 1.0) in the Cartesian coordinate system [37–39]. Equation (1) alternatively yields the following dis-

tribution of magnetization density:

$$M_x(\mathbf{r} + \mathbf{R}) = M_x(\mathbf{r})\cos(2\pi\mathbf{q}\cdot\mathbf{R}) - M_y(\mathbf{r})\sin(2\pi\mathbf{q}\cdot\mathbf{R}),$$
$$M_y(\mathbf{r} + \mathbf{R}) = M_x(\mathbf{r})\sin(2\pi\mathbf{q}\cdot\mathbf{R}) + M_y(\mathbf{r})\cos(2\pi\mathbf{q}\cdot\mathbf{R}),$$
$$M_z(\mathbf{r} + \mathbf{R}) = M_z(\mathbf{r}). \qquad (2)$$

As a result, $\mathbf{q}$ dictates the phase difference between mag-netic moments related by $\mathbf{R}$, corresponding to a relative ro-tation about the $\mathbf{z}$ axis by a degree of $2\pi\mathbf{q}\cdot\mathbf{R}$. In the rutile primitive cell, the Cartesian axes $\mathbf{x}$, $\mathbf{y}$, $\mathbf{z}$ are brought parallel to three lattice bases $\mathbf{a}$, $\mathbf{b}$, $\mathbf{c}$, respectively. Given a vanishing z component, spins lie and rotate in the c-plane. Figures 1(a)–1(d) show some examples of the allowed spiral states with $\mathbf{q} = (0, 0, 0)$ and $(0, 0, 0.5)$ in reciprocal bases $\mathbf{a}^*$, $\mathbf{b}^*$, $\mathbf{c}^*$. As can be easily checked, the red and yellow spins separated by a full lattice vector $\mathbf{c}$ are crossed at an angle of $\gamma = 2\pi\mathbf{q}\cdot\mathbf{c}$. In contrast, the angle α between red and blue spins is not explicitly constrained by $\mathbf{q}$ because they are not separated by a lattice vector. Consequently, two nondegenerate states are formed for each wave vector.

The experimental spiral wave vector of β-MnO$_2$ ($\mathbf{q}_{\text{exp}}$) is $(0, 0, 2/7)$. As shown in Figs. 1(e) and 1(f), the two intracell spins (1 and 1′) are situated at the corner and body center with $\alpha = 5\pi/7 \approx 129°$. Both of them rotate by a step of $\gamma = 4\pi/7 \approx 103°$ from cell 1 (1′) to cell 7 (7′) consecutively, thus spanning two full circles for every seven unit cells [21,40]. The angle between blue and yellow spins denoted as β satisfies

$$\alpha + \beta + \gamma = 2\pi, \qquad (3)$$

which leads to $\beta = \alpha = 5\pi/7$ in this case.

Following the above analysis, a specific spiral state is well defined by a ($\mathbf{q}$, α) pair. Computationally, one needs to fix $\mathbf{q}$ and initialize α as α_0 (specify the two magnetic moments) for a single calculation. After structural optimization, the self-consistent value of α can be extracted from the charge-density distribution, which does not equal to α_0 in most situations. We sample $\mathbf{q}$ along the Γ $(0, 0, 0)$-Z $(0, 0, 0.5)$ path and start with $\alpha_0 = 0°, 90°, 180°$ separately to cover as many spiral states as possible. For the reason that $\alpha_0 = 0°$ tends to result in much higher energy, only the dispersions of $\alpha_0 = 90°$ and $180°$ are shown in Fig. 1(g), together with the final configurations of three characteristic spin vectors.

The two setups are degenerate in both energy and spin order for $q_c = 0 \sim 0.4$. Overall, $\alpha_0 = 90°$ produces contin-uously changing spiral states, with the blue spin rotating anticlockwise from Γ (antiferromagnetic, AFM, $\alpha = 180°$) to Z (helix, $\alpha = 90°$) gradually. Therefore, the energy dispersion is smooth in the whole range. For $\alpha_0 = 180°$, however, the blue spin starts to turn back around $q_c = 0.45$ and undergoes an abrupt change on reaching the Z point. Finally, $\alpha = 180°$ is obtained again in a more stable double-AFM (DAFM) state, inflecting the dispersion downwards. Note that in the neighborhood of the Z point, e.g., $q_c = 0.45$, the small energy difference also stems from distinct self-consistent states (dif-ferent α) instead of numerical errors or failure in convergence.

We also computed the energy at $\mathbf{q}_{\text{exp}}$ (blue circle), which lies very close to the minimum of the curve. More importantly, α spontaneously converges to the experimental value of $129°$. In this sense, the experimentally determined helical spin order can be predicted with high accuracy, which verifies the power

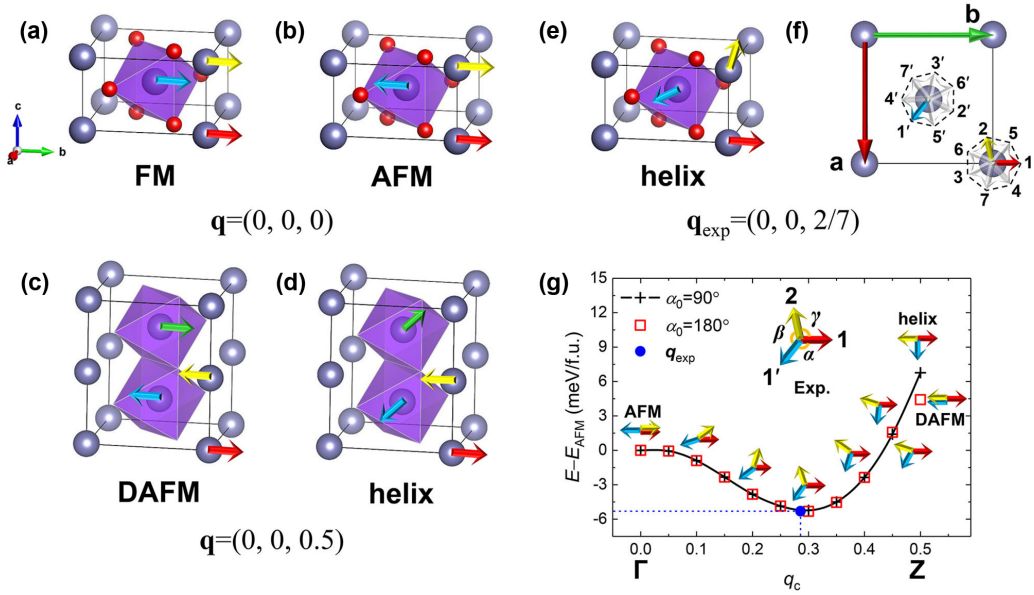FIG. 1. (a)–(f) Magnetic supercells for different spiral states of β-MnO$_2$, uniquely determined by **q** and α. Arrows on atoms represent local magnetic moments. Collinear ferromagnetic [FM, (a)] and antiferromagnetic [AFM, (b)] states correspond to **q** = (0, 0, 0) (Γ point) with $\alpha = 0°$ and 180° respectively. At **q** = (0, 0, 0.5) (Z point), the collinear state double-AFM [DAFM, (c)] is characterized by $\alpha = 180°$ or 0°, the noncollinear spin helix (d) by $\alpha = 90°$. The experimental helical magnetism [**q** = (0, 0, 2/7), $\alpha = 129°$] is demonstrated in the primitive cell (e) and its plan view (f). (g) Computed spiral dispersions along the Γ-Z path with $\alpha_0 = 0°$ and 90° separately, where the energy is scaled to a formula unit with respect to the AFM type.

of the full-anisotropy strategy. Special spiral states at the Γ and Z points have also been produced by varying the initial input α_0. Based on these findings, we will continue to explore the ground states and physical insights of recently discovered rutile-type FeO$_2$.

IV. MAGNETIC GROUND STATES OF RUTILE-TYPE FeO$_2$

A. Global search for spiral states

We expand the sampling area of spin-spiral calculations to a complete high-symmetry k path. The generalized Bloch theorem guarantees the efficiency of searching for the spiral-modulated ground states on a primitive-cell basis. It has been extensively reported that the tetragonal rutile structure ($P4_2/mnm$) typically undergoes a second-order phase transition into the orthorhombic CaCl$_2$-type ($Pnnm$) structure at high pressure [41–43]. This structural distortion only involves octahedral rotation around the **c** axis, which easily fits into the wave-vector search.

Figure 2 shows spiral dispersions of FeO$_2$ along the rutile high-symmetry k path. At 0 GPa [Fig. 2(a)], the tetragonal symmetry is stabilized in a high-spin (HS) state. The global energy minimum is reached at Z (0, 0, 0.5), with the DAFM ($\alpha = 0°$ or 180°) rather than helical ($\alpha = 90°$) spin order [Figs. 1(c) and 1(d)]. Another local minimum appears at A (0.5, 0.5, 0.5), with energy only slightly higher than DAFM. When the volume is compressed to 27.5 Å^3/f.u. [Fig. 2(b)], orthorhombic distortion becomes favorable throughout the whole path, introducing an energy gain of about 16.0 meV/f.u. on average. Note that neither the overall pattern of the dispersions nor the spin state is changed despite notable octahedral rotation (see Sec. IV B). Therefore, the collinear DAFM spin order persists in the HS state.

The spin-state transition (SST) occurs on further compression, accompanied by dramatic changes in the dispersions. As shown in Figs. 2(c) and 2(d), the energy becomes less dispersed on the whole, with the ground-state wave vector deviating from the Z point yet remaining in the Γ-Z path. This corresponds to a spin spiral propagating in the **c** direction, which is similar to the ambient-pressure β-MnO$_2$ phase. The orthorhombic distortion is still preferred in the high-pressure low-spin (LS) regime, whose energy gain broadens from 1.9 meV/f.u. (25 Å^3/f.u.) to 12.3 meV/f.u. (24 Å^3/f.u.). In the latter case, the magnitude is actually comparable to the spread of magnetic energy. To determine the ground-state wave vector more accurately, calculations with increased sampling density are conducted along the Γ-Z segment [Figs. 2(e) and 2(f)]. For both volumes, the energy minimizes at $\mathbf{q}_{min} =$ (0, 0, 0.33) with $\alpha \approx 120°$, that is to say, every 3 unit cells along the **c** axis constitutes a period of such a spin helix.

It is worth to note that the special states in Figs. 1(a)–1(d) are again obtained at high-symmetry points in these dispersions. The starting angle α_0 is important for inducing possible metastable states because it imposes constraints on the initial charge-density distribution. Given the wave vector is fixed, the optimization algorithm may either end up at a nearby local minimum if it exists or overcome the energy barrier towards the global minimum. In the vicinity of high-symmetry points, this competition sometimes makes the algorithm less stable and efficient, yielding discontinuous singular states such as the one next to the Γ point in Fig. 2(d).

In nature, this correlated many-body system exhibits competitions between fluctuated spiral states. Although the ground-state spin order is closely related to the spin state, the octahedral rotation seems to be decoupled from magnetic transitions.
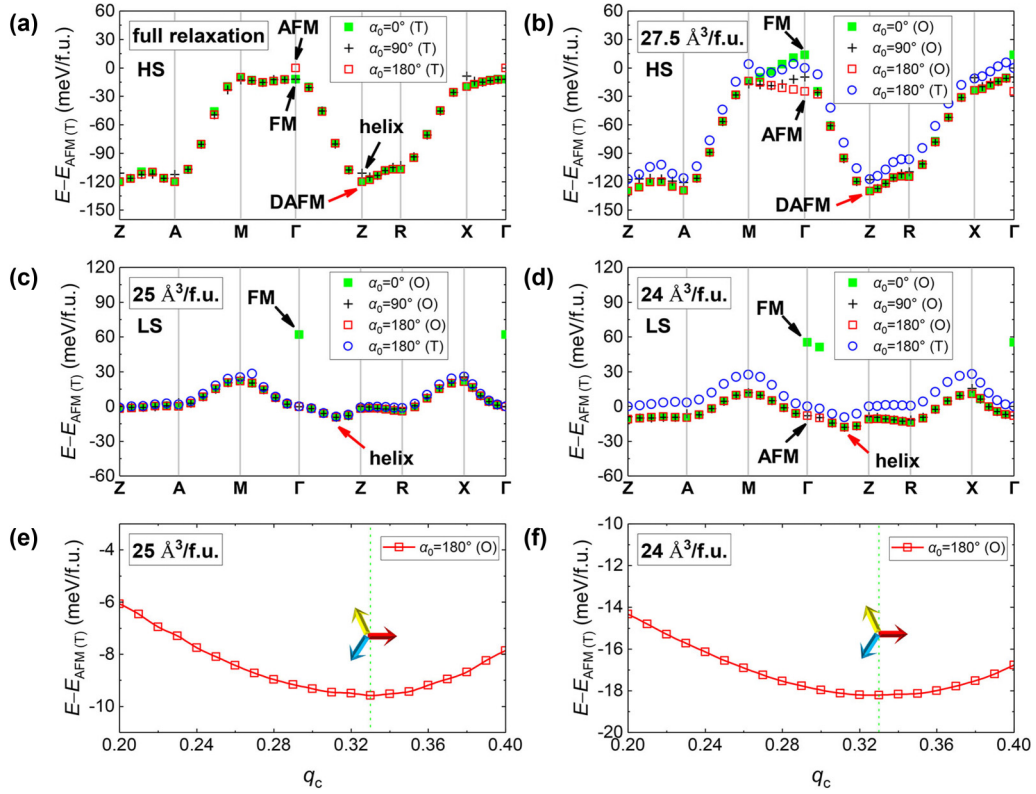
FIG. 2. Spiral dispersions along the rutile high-symmetry k path calculated with (a) full relaxation, corresponding to 0 GPa, or with the volume fixed at (b) 27.5 Å^3/f.u., (c) 25 Å^3/f.u., and (d) 24 Å^3/f.u., representing increasing pressures. (a) and (b) are computed in a HS state whereas (c) and (d) in a LS state. The spin-spiral search starts with $\alpha_0 = 0°$, 90°, and 180° separately for the ambient-pressure tetragonal (T) phase and high-pressure orthorhombic (O) phase. The global ground states (red arrow) together with some other special states (black arrow) are indicated. For comparison, dispersions of the less stable tetragonal phase at high pressures are also given with $\alpha_0 = 180°$. Figures 2(e) and 2(f) are magnified Γ-Z segments of the orthorhombic ($\alpha_0 = 180°$) dispersions in Figs. 2(c) and 2(d), respectively, with increased sampling density. Energies are scaled to a formula unit with respect to the tetragonal AFM (Γ point, $\alpha = \alpha_0 = 180°$) phases.

B. Magnetic transition and structural distortion

As discussed earlier, two independent pressure-induced phase transitions seem to exist in the FeO$_2$ system: the orthorhombic distortion at a relatively lower pressure and the magnetic phase transition at a higher pressure. Two magnetic ground states have been revealed from the global search, namely HS-DAFM [$\mathbf{q} = (0, 0, 0.5)$, $\alpha = 0°$ or 180°] and LS-helix [$\mathbf{q} = (0, 0, 0.33)$, $\alpha \approx 120°$]. Therefore, we will focus on the magnetic transition first. With the spin orders fixed, energy-volume relations in the HS and LS regimes are calculated and fitted separately [Fig. 3(a)] using the Birch-Murnaghan isothermal equation [33]:

$$E(V) = E_0 + \frac{9V_0 B_0}{16} \left\{ \left[\left(\frac{V_0}{V} \right)^{2/3} - 1 \right]^3 B'_0 + \left[\left(\frac{V_0}{V} \right)^{2/3} - 1 \right]^2 \left[6 - 4 \left(\frac{V_0}{V} \right)^{2/3} \right] \right\}, \quad (4)$$

where E_0 is the equilibrium energy, V_0 is the equilibrium volume, B_0 is the bulk modulus, and B'_0 is the derivative of the bulk modulus with respect to pressure.

We can draw a line which is tangent to both fitting curves, and the critical pressure p_{c2} is found by taking the opposite of its slope. Alternatively, p_{c2} may be directly determined from

the enthalpy-pressure diagram (inset) derived from the E-V relations:

$$H = E + pV = E - V \left(\frac{\partial E}{\partial V} \right)_S. \quad (5)$$

The intersection of the two H-p curves defines a critical pressure of 22 GPa, which remains a constant in the two-phase zone according to the Gibbs phase rule.

The average magnitude of the magnetic moments of Fe is also given in Fig. 3(a). At 0 GPa (31 GPa), the values are around 3.50 μ_B(1.75 μ_B), corresponding to the HS (LS) state of Fe^{4+}[$3d^4$]. The SST results from the competition between the splitting energy (Δ) and electron pairing energy (P) within the crystal-field theory (CFT) framework. The compression induces a contraction in bond lengths and enhances the repulsion between e_g orbitals and O ligands, thus broadening the splitting gap. If it outweighs the electron pairing energy ($\Delta > P$), the LS state will be energetically more favorable.

The magnetic transition is predicted to be of first order because of the discontinuity in volume (from V_1 to V_2) at p_{c2}. However, the widely studied orthorhombic distortion of the rutile structure is of second order in nature [41–43]. This lower critical pressure p_{c1} may be conveniently deduced from extrapolation of pressure-dependent structural parameters. As illustrated in Fig. 3(c), the orthorhombic distortion is realized
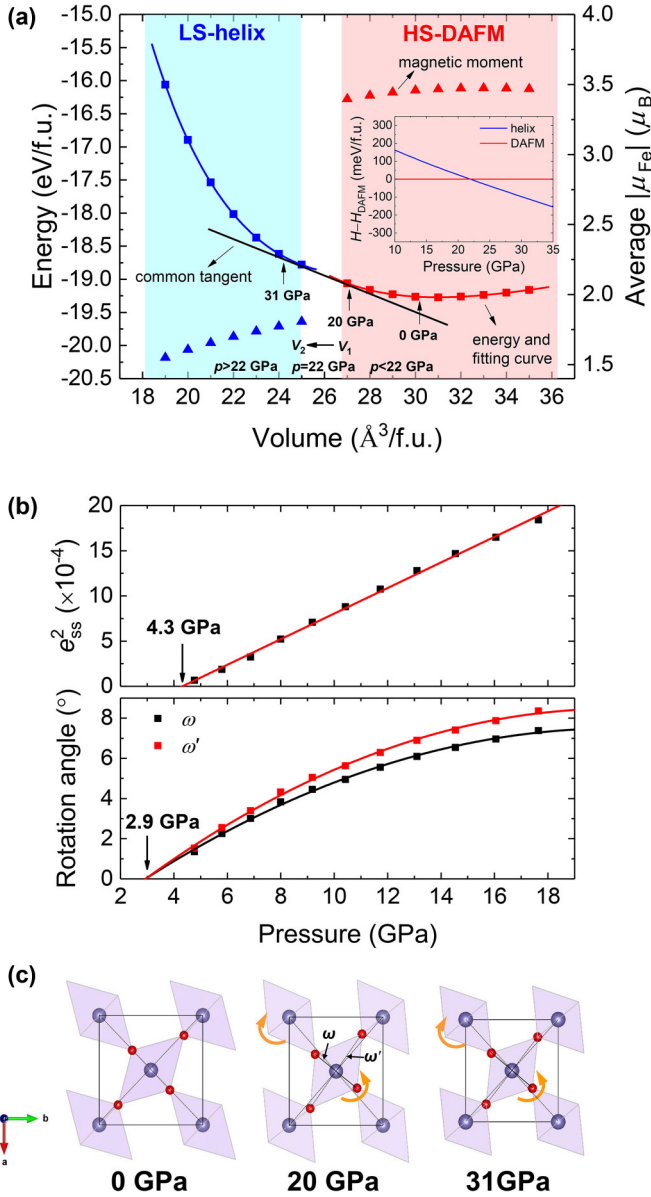
FIG. 3. (a) Total energy (square) and average magnitude of the magnetic moments of Fe (triangle), as a function of volume. The energy-volume relations are fitted with the Birch-Murnaghan EOS, and then converted to enthalpy-pressure curves (inset) to determine the critical pressure of the magnetic phase transition (p_{c2}). (b) The spontaneous strain and octahedral rotation angles in the HS orthorhombic phase as a function of pressure, fitted by linear and quadratic functions, respectively. The critical pressure of the orthorhombic distortion (p_{c1}) is obtained by extrapolation. (c) Structural evolution across the two phase transitions, represented by structures at 0, 20, and 31 GPa.

through octahedral rotation around the **c** axis. The two rotation angles denoted as ω and ω' increase with pressure, as well described by quadratic fitting curves in the lower panel of Fig 3(b). Extrapolation to the p axis yields a critical pressure of 2.9 GPa for the onset of octahedral rotation. Another structural parameter characterizing the distortion is the spontaneous

TABLE I. Bond lengths and bond valences for the ambient FeO$_2$ phase.

Bond[a]	Bond length (Å)	Bond valence	Bond valence sum
Fe–O1 (e)	1.836	0.841	Fe: 4.134
Fe–O2 (e)	1.844	0.823	O: 2.067
Fe–O3 (a)	2.108	0.403	

[a](e) and (a) stand for equatorial and apical oxygen atoms, respectively. Each bond contributes twice to the bond valence sum of Fe and once to that of O.

strain in the ferroelastic orthorhombic phase, given by

$$e_{ss} = \frac{a - b}{a + b}. \tag{6}$$

This order parameter should be linearly proportional to $(p - p_c)^{1/2}$ according to Landau's theory of second-order phase transitions [44]. In the upper panel of Fig. 3(b), the e_{ss}^2 vs p relation is plotted and a rather good linear fit is obtained, which similarly yields $p_{c1} = 4.3$ GPa through extrapolation. In comparison, this critical pressure has been found to be 0.9 GPa for β-MnO$_2$ [42] and 12 GPa for CrO$_2$ [44] by the same token but based on experimental data.

Besides octahedral rotation, octahedral elongation along one of the $\langle 110 \rangle$ directions has also been observed in the HS states [Fig 3(c)]. At ambient pressure, the Fe–O bond lengths for apical and equatorial O are 2.11 and 1.84 Å, respectively (Table I), corresponding to a relative elongation of 14.7%. The strong Jahn-Teller effect of the HS Fe^{4+} ions should well account for this elongation, which weakens with increasing pressure and vanishes upon the SST.

C. Chemical bonding and electronic structures

In chemistry, the formal oxidation state based on electron counting is a powerful concept to understand chemical bonding [45]. Pyrite-type FeO$_2$ was first proposed as a peroxide where the covalent O–O bonds facilitate the forming of Fe^{2+} as in the case of FeS$_2$. Later theoretical studies held the view that the valence of iron is $+(2 + \delta)(0 < \delta < 1)$ or close to +3 [14,17,46], including one work using Bader charge analysis. Although the charge-partitioning scheme is totally compatible with first-principles calculations, it tends to underestimate the valences quantitatively for most compounds. For example, the Bader charges assigned to Fe and O in Fe$_2$O$_3$ are only +1.75 and −1.17, respectively [17]. In addition, the differences between various stoichiometries are not obvious enough, raising ambiguity to some degree.

For rutile-type FeO$_2$, an oxidation state of +4 is anticipated in analogy to other rutile compounds, which is also supported by our previous discussion of spin states and the Jahn-Teller distortion. Here, we resort to the bond valence model [34] to examine whether Fe^{4+} complies with the rutile structure instead of performing charge-partitioning procedures. Bond valences in the ambient phase (Table I) are calculated with relaxed bond lengths and the empirical bond valance parameter for Fe^{4+}–O (1.772) derived from the CaFeO$_3$ phase [47]. In fact, the bond valence parameter is dependent on
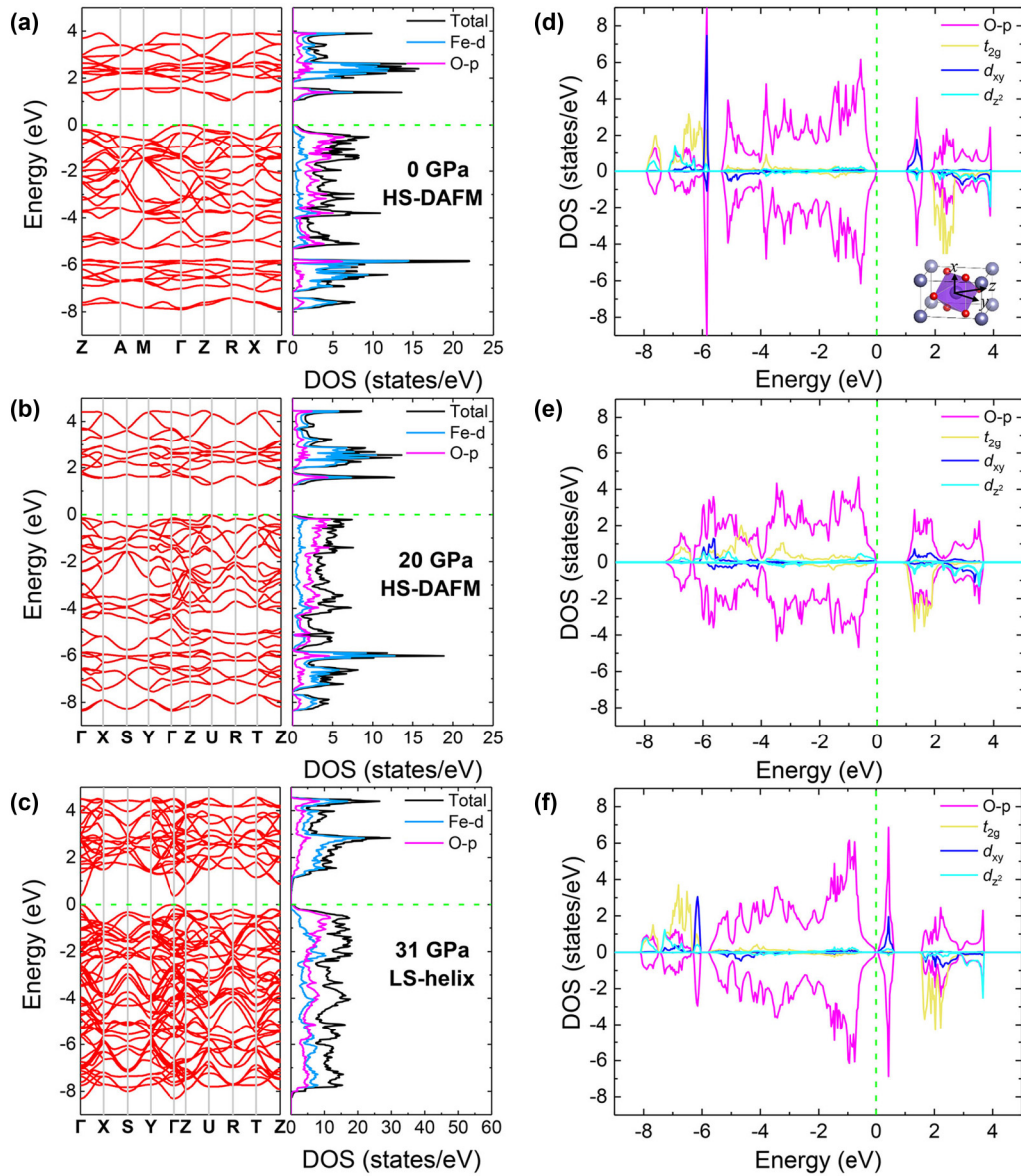
FIG. 4. Total, Fe-d projected, O-p projected DOS, and corresponding band dispersions of (a) tetragonal HS-DAFM phase at 0 GPa, (b) orthorhombic HS-DAFM phase at 20 GPa, and (c) orthorhombic LS-helix phase at 31 GPa. Only one spinor is shown in (a) and (b) because the other one has the same energy dispersion. (d) DOS projected to O-p orbitals and the t_{2g}, d_{xy}, d_{z^2} orbitals of a spin-up Fe for the phase at 0 GPa, with respect to the CFT coordinate system (inset) [50]. With fixed lattice parameters, two imaginary states are simulated for comparison, where (e) Hubbard U is reduced to 2.5 eV or (f) the oxygen atoms are deliberately displaced to suppress the Jahn-Teller distortion.

the oxidation state. Thus as a general rule, bond valence sums that agree with the assumed formal valence can be taken as primary evidence of a correct structure [34]. Due to the Jahn-Teller distortion, the central Fe atom in an [FeO$_6$] octahedron bonds with 2 apical and 4 equatorial O atoms. The bond valence sums for Fe (4.134) and O (2.067) turn out to match the assumed oxidation states quite well, suggesting correctness of this distorted structure. The bond valences for high-pressure phases are not given because the bond valence parameter is also impacted by pressure [48].

For condensed matter, the extended band structure is somewhat more accepted in the physical world. As indicated in Fig. 4(a), the ambient ground state is an insulator with an in-

direct band gap of about 1.03 eV. The valence-band maximum and conduction band minimum are located at Γ (0, 0, 0) and near R (0.5, 0.5, 0), respectively. The main contribution to the valence bands (VBs) is O-p orbitals while the very narrow conduction bands (CBs) show strong hybridization between O-p orbitals and Fe-d orbitals. According to the Hubbard model [49], electron correlation splits the d bands into the lower Hubbard band (LHB) below VB, and the upper Hubbard band (UHB) above CB. Raising the pressure to 20 GPa introduces second-order symmetry breaking and results in band dispersions along the different orthorhombic high-symmetry k path [Fig. 4(b)]. However, the indirect band gap persists under compression and octahedral rotation, even broadened by 0.2
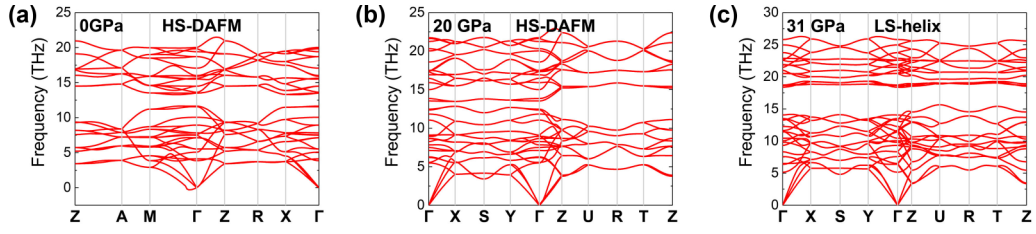
FIG. 5. Phonon dispersions of (a) tetragonal HS-DAFM phase at 0 GPa, (b) orthorhombic HS-DAFM phase at 20 GPa, (c) orthorhombic LS-helix phase at 31 GPa.

eV. With similar patterns, the density of states (DOS) exhibits larger bandwidths of VB, UHB, and LHB due to increased orbital overlap. After the SST, the electronic structure undergoes a major change. The band gap becomes direct at the Γ point and reduces to 0.35 eV [Fig. 4(c)]. Both VB and CB are better dispersed with continuity. Mixed O-p and Fe-d states now dominate the VB, with the original narrow CB absent from above the Fermi level.

Electron correlation, lattice distortion, and magnetism are key to understanding the intricate electronic properties of strongly correlated systems, such as V_2O_3, VO_2, which are known for the temperature-driven MIT [1]. These competing factors also exist in the current FeO_2 system, only the driving force being pressure. In Fig. 4(d), we project DOS of the HS-DAFM (0 GPa) phase to five d orbitals of a spin-up Fe^{4+} with respect to the crystal-field coordinate system (inset) [50]. Although the octahedra in this structure deviate from the formal O_h symmetry, we will still use the t_{2g} and e_g notations for convenience. The major d component in the narrow CB is d_{xy} of e_g symmetry, indicating σ interaction with O-p orbitals [13,51]. To understand this curious CB structure, the same site-and-orbital-projected DOS of two imaginary states are calculated for comparison. In the one with weakened electron correlation ($U = 2.5$ eV, $J = 0.8$ eV), the LHB moves

to higher energy levels and becomes more hybridized with p bands [Fig. 4(e)]. Conversely, the t_{2g} bands above the Fermi level move to lower energy, mixing with and flattening out the narrow d_{xy}-p bands. When applying the original parameters $U = 5$ eV, $J = 0.8$ eV but deliberately suppressing the Jahn-Teller distortion in the relaxed structure, the gap between the d_{xy}-p bands and t_{2g} bands remains [Fig. 4(f)]. Nonetheless, the actual band gap is smeared by O-p states, which implies that the Jahn-Teller distortion is essential to opening a band gap in the HS phases despite considerable electron correlation.

There is no sign of previously reported half metallicity in our calculations, which is actually the effect that comes with ferromagnetic ordering, as also highlighted in the VO_2 case [52].

D. Dynamical stability

In addition to obvious energetic advantage, the orthorhombic distortion introduces further stability on the dynamical level. As indicated in Figs. 5(b) and 5(c), the phonon dispersions at 20 and 31 GPa both show a linear behavior near the Γ point. No imaginary frequencies are observed along the high-symmetry k path, suggesting their dynamical stability against thermal vibrations. By contrast, the tetragonal HS-DAFM (0

TABLE II. Elastic constant tensor (c_{ij}) its minimum eigenvalue (λ_1), bulk modulus (B), shear modulus (G), Young's modulus (E), and Possion's ratio (ν) for the three phases at 0, 20, and 31 GPa. All the values are given in GPa except for ν and the underlined values in (c_{ij}) are independent components for the given symmetry.

Phase	Symmetry	(c_{ij})						λ_1	B	G	E	ν
HS-DAFM (0 GPa)	Tetragonal	$\underline{123}$ 88 89 0 0 0	88 123 89 0 0 0	89 89 $\underline{383}$ 0 0 0	0 0 0 $\underline{78}$ 0 0	0 0 0 0 78 0	0 0 0 0 0 $\underline{114}$	34	117	63	160	0.272
HS-DAFM (20 GPa)	Orthorhombic	$\underline{292}$ 158 161 0 0 0	158 $\underline{220}$ 107 0 0 0	161 107 $\underline{446}$ 0 0 0	0 0 0 $\underline{76}$ 0 0	0 0 0 0 $\underline{100}$ 0	0 0 0 0 0 $\underline{188}$	76	193	97	250	0.285
LS-helix (31 GPa)	Orthorhombic	$\underline{495}$ 300 265 0 0 0	300 $\underline{392}$ 185 0 0 0	265 185 $\underline{579}$ 0 0 0	0 0 0 $\underline{168}$ 0 0	0 0 0 0 $\underline{190}$ 0	0 0 0 0 0 $\underline{317}$	135	323	163	417	0.285

GPa) phase goes through a minor phonon softening near the Γ point yet is very stable in other regions [Fig. 5(a)]. We also calculate the elastic constant tensors and some related mechanical properties for these structures (Table II). Indicated by positive minimum eigenvalues, the elastic constant tensors are all positive-definite matrices. Therefore, the three phases exhibit a certain degree of mechanical stability, that is, the ability to endure a random strain or deformation.

V. CONCLUSIONS

We first revisit the classical β-MnO$_2$ system of helical magnetism and successfully reproduce the experimental spiral wave vector from a dispersion curve, which in turn justifies the predictive power of the fully anisotropic DFT+U method used in this study. By employing the same scheme, magnetic ground states varying with pressure are explored for the recently discovered isostructural rutile-type FeO$_2$. We have identified a second-order CaCl$_2$-type orthorhombic distortion starting from $3 \sim 4$ GPa, which is characterized by octahedral rotation. The energetically and dynamically more stable orthorhombic phase further undergoes a first-order magnetic transition from the collinear HS-DAFM phase to the non-collinear LS-helix phase at about 22 GPa. Electronic properties also change tremendously upon the spin-state transition. For the HS states, an indirect band gap of about 1 eV is formed along with the narrow d_{xy}-p hybridized CB, through electron correlation and the Jahn-Teller effect. This character does not persist up to the LS state, whose direct band gap is around 0.35 eV at 31 GPa. The magnetic moments, Jahn-Teller distortion, and bond valence sums consistently indicate a $+4$ oxidation state of Fe instead of $+(2 + \delta)(0 < \delta < 1)$ as in pyrite-type FeO$_2$. Our work enriches the phase diagram of iron dioxides with physical insights, and the way we approach magnetism can be promisingly generalized to other strongly correlated systems with spin spirals.

[1] M. Imada, Rev. Mod. Phys. **70**, 1039 (1998).

[2] H. Y. Hwang, Y. Iwasa, M. Kawasaki, B. Keimer, N. Nagaosa, and Y. Tokura, Nat. Mater. **11**, 103 (2012).

[3] M. Born and K. Huang, *Dynamical Theory of Crystal Lattices* (Clarendon Press, Oxford, 1954).

[4] D. A. H. Hanaor and C. C. Sorrell, J. Mater. Sci. **46**, 855 (2010).

[5] T. Hyeon, S. S. Lee, J. Park, Y. Chung, and H. B. Na, J. Am. Chem. Soc. **123**, 12798 (2001).

[6] H. Shokrollahi, J. Magn. Magn. Mater. **426**, 74 (2017).

[7] D. C. Cronemeyer, Phys. Rev. **87**, 876 (1952).

[8] J. Pascual, J. Camassel, and H. Mathieu, Phys. Rev. B **18**, 5606 (1978).

[9] A. L. Linsebigler, G. Lu, and J. T. Yates, Chem. Rev. **95**, 735 (1995).

[10] Y. Fan, G. Hu, S. Yu, L. Mai, and L. Xu, Sci. China Mater. **62**, 325 (2018).

[11] J. M. D. Coey and M. Venkatesan, J. Appl. Phys. **91**, 8345 (2002).

[12] S. A. Wolf, D. D. Awschalom, R. A. Buhrman, J. M. Daughton, S. v. Molnar, M. L. Roukes, A. Y. Chtchelkanova, and D. M. Treger, Science **294**, 1488 (2001).

[13] K. Liu, S. Lee, S. Yang, O. Delaire, and J. Wu, Mater. Today **21**, 875 (2018).

[14] Q. Hu, D. Y. Kim, W. Yang, L. Yang, Y. Meng, L. Zhang, and H. K. Mao, Nature (London) **534**, 241 (2016).

[15] Q. Hu, D. Y. Kim, J. Liu, Y. Meng, L. Yang, D. Zhang, W. L. Mao, and H. K. Mao, Proc. Natl. Acad. Sci. U.S.A. **114**, 1498 (2017).

[16] B. G. Jang, D. Y. Kim, and J. H. Shim, Phys. Rev. B **95**, 075144 (2017).

[17] C. Lu, M. Amsler, and C. Chen, Phys. Rev. B **98**, 054102 (2018).

[18] M. Tang, Z.-W. Niu, X.-L. Zhang, and L.-C. Cai, J. Alloys Compd. **765**, 271 (2018).

[19] B. G. Jang, J. Liu, Q. Hu, K. Haule, H.-K. Mao, W. L. Mao, D. Y. Kim, and J. H. Shim, Phys. Rev. B **100**, 014418 (2019).

[20] D. A. Kitchaev, H. Peng, Y. Liu, J. Sun, J. P. Perdew, and G. Ceder, Phys. Rev. B **93**, 045132 (2016).

[21] H. Sato, T. Enoki, M. Isobe, and Y. Ueda, Phys. Rev. B **61**, 3563 (2000).

[22] C. Franchini, R. Podloucky, J. Paier, M. Marsman, and G. Kresse, Phys. Rev. B **75**, 195128 (2007).

[23] A. I. Liechtenstein, V. I. Anisimov, and J. Zaanen, Phys. Rev. B **52**, R5467 (1995).

[24] J. P. Perdew, K. Burke, and M. Ernzerhof, Phys. Rev. Lett. **77**, 3865 (1996).

[25] P. E. Blöchl, Phys. Rev. B **50**, 17953 (1994).

[26] G. Kresse and J. Furthmüller, Phys. Rev. B **54**, 11169 (1996).

[27] G. Kresse and J. Furthmiiller, Comput. Mater. Sci. **6**, 15 (1996).

[28] S. L. Dudarev, G. A. Botton, S. Y. Savrasov, C. J. Humphreys, and A. P. Sutton, Phys. Rev. B **57**, 1505 (1998).

[29] J. S. Lim, D. Saldana-Greco, and A. M. Rappe, Phys. Rev. B **94**, 165151 (2016).

[30] D. A. Tompsett, D. S. Middlemiss, and M. S. Islam, Phys. Rev. B **86**, 205126 (2012).

[31] H. J. Monkhorst and J. D. Pack, Phys. Rev. B **13**, 5188 (1976).

[32] L. M. Sandratskii, J. Phys.: Condens. Matter **3**, 8565 (1991).

[33] F. Birch, Phys. Rev. **71**, 809 (1947).

[34] I. D. Brown, *The Chemical Bond in Inorganic Chemistry: The Bond Valence Model* (Oxford University Press, Oxford, 2016), Vol. 27.

[35] R. Yu, J. Zhu, and H. Q. Ye, Comput. Phys. Commun. **181**, 671 (2010).

[36] D. Alfè, Comput. Phys. Commun. **180**, 2622 (2009).

[37] K. Knöpfle, L. M. Sandratskii, and J. Kübler, Phys. Rev. B **62**, 5564 (2000).

[38] M. Marsman and J. Hafner, Phys. Rev. B **66**, 224409 (2002).

[39] E. Sjöstedt and L. Nordström, Phys. Rev. B **66**, 014447 (2002).

[40] A. Yoshimori, J. Phys. Soc. Jpn. **14**, 807 (1959).

[41] J. Haines and J. M. Léger, Phys. Rev. B **55**, 11144 (1997).

[42] J. Haines, J. M. Léger, and S. Hoyau, J. Phys. Chem. Solids **56**, 965 (1995).

[43] A. Togo, F. Oba, and I. Tanaka, Phys. Rev. B **78**, 134106 (2008).

[44] B. R. Maddox, C. S. Yoo, D. Kasinathan, W. E. Pickett, and R. T. Scalettar, Phys. Rev. B **73**, 144111 (2006).

[45] A. Walsh, A. A. Sokol, J. Buckeridge, D. O. Scanlon, and C. R. A. Catlow, Nat. Mater. **17**, 958 (2018).

[46] S. S. Streltsov, A. O. Shorikov, S. L. Skornyakov, A. I. Poteryaev, and D. I. Khomskii, Sci. Rep. **7**, 13005 (2017).

[47] P. M. Woodward, D. E. Cox, E. Moshopoulou, A. W. Sleight, and S. Morimoto, Phys. Rev. B **62**, 844 (2000).

[48] J. D. Jorgensen, S. Pei, P. Lightfoot, D. G. Hinks, B. W. Veal, B. Dabrowski, A. P. Paulikas, and R. Kleb, Physica C **171**, 93 (1990).

[49] J. Hubbard, Proc. R. Soc. London, Ser. A **276**, 238 (1963).

[50] X. Yuan, Y. Zhang, T. A. Abtew, P. Zhang, and W. Zhang, Phys. Rev. B **86**, 235103 (2012).

[51] P. I. Sorantin and S. Karlheinz, Inorg. Chem. **31**, 567 (1992).

[52] S. Xu, X. Shen, K. A. Hallman, R. F. Haglund, and S. T. Pantelides, Phys. Rev. B **95**, 125105 (2017).